Inorganic Chemistry
Article
pubs.acs.org/IC

Impact of Mn^{3+} upon Structure and Magnetism of the Perovskite Derivative $Pb_{2-x}Ba_xFeMnO_5$ ($x \sim 0.7$)

N. Barrier,[*,†] O. I. Lebedev,[†] Md. Motin Seikh,[†,§] F. Porcher,[‡] and B. Raveau[†]

[†]Laboratoire CRISMAT, UMR 6508 CNRS, ENSICAEN, 6 bd du Maréchal Juin, 14050 CAEN Cedex 4, France
[‡]CEA, Centre de Saclay, DSM/IRAMIS, Laboratoire Leon Brillouin (LLB), F-91191 Gif-sur-Yvette, France

Supporting Information

ABSTRACT: On the basis of the Mn^{3+} for Fe^{3+} substitution in $Pb_{2-x}Ba_xFe_2O_5$, a novel oxide $Pb_{1.3}Ba_{0.7}MnFeO_5$ has been synthesized at normal pressure. Though it belongs to the same structural family, the mixed "MnFe" oxide exhibits a very different structural distortion of its framework compared to the pure "Fe_2" oxide, due to the Jahn−Teller effect of Mn^{3+}. Combined neutron diffraction, high resolution electron microscopy/high angle annular dark field−scanning transmission electron microscopy (HAADF−STEM) investigations allow the origin of this difference to be determined. Here we show that the MO_6 octahedra of the double perovskite layers in the "MnFe" structure exhibit a strong tetragonal pyramidal distortion "5 + 1", whereas the "Fe_2" structure shows a tetrahedral distortion "4 + 2" of the FeO_6 octahedra. Similarly, the MO_5 polyhedra of the "MnFe" structure tend toward a tetragonal pyramid, whereas the FeO_5 polyhedra of the "Fe_2" structure are closer to a trigonal bipyramid. Differently from the oxide $Pb_{2-x}Ba_xFe_2O_5$, which is antiferromagnetic, the oxide $Pb_{1.3}Ba_{0.7}MnFeO_5$ exhibits a spin glass behavior with $T_g \sim 50$ K in agreement with the disordered distribution of the Mn^{3+} and Fe^{3+} species.

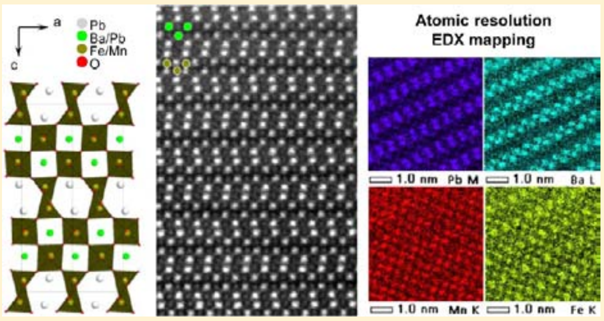

INTRODUCTION

The discovery 15 years ago of the $Pb_{1.33}Sr_{0.67}Fe_2O_5$ structure[1] has opened the route to the exploration of several series of ferrites closely related to the perovskite, with a similar formulation to that of the brownmillerite family $Ca_2Fe_2O_5$ or $Sr_2Fe_2O_5$,[2,3] but with different iron polyhedra interconnecting the FeO_6 octahedra, i.e., FeO_5 tetragonal pyramids or trigonal bipyramids instead of FeO_4 tetrahedra. In this way, the "$Pb_2Fe_2O_5$" perovskites were studied,[4] whereas more recently the oxides $Pb_{2-x}Ba_xFe_2O_5$[5] and $Pb_{1.33}Sr_{0.67-x}Ba_xFe_2O_5$[6] were shown to be isotypic to the Sr-phase and to exhibit an antiferromagnetic structure below 625 K. Trivalent manganese, due to its Jahn−Teller properties, should be able to sit in both sites, octahedral and pyramidal, and consequently is a potential candidate for generating similar structures. In fact, iron-free manganites related to this structural family could not be synthesized previously under normal pressure conditions. However, high pressure synthesis allowed a mixed valent, Mn^{3+}/Mn^{4+}, manganite $PbMnO_{2.75}$[7] and a pure trivalent manganite $Pb_2Mn_2O_5$[8] to be synthesized. Importantly, this second phase, $Pb_2Mn_2O_5$, was shown to belong to the same structural family as the $Pb_{2-x}A_xFe_2O_5$ ferrites[1,5,6] raising the issue of the role of Mn^{3+} and Fe^{3+} cations in the stabilization of such a structure.

In order to understand the different behavior of manganese with respect to iron in this structural family, we have investigated the possibility to synthesize similar manganoferrites, but at normal pressure. Here we report on the oxide $Pb_{1.3}Ba_{0.7}MnFeO_5$, which combined neutron powder diffraction (NPD) and high resolution electron microscopy (HREM) study, shows a different distortion of its octahedral layers compared to $Pb_{1.3}Ba_{0.7}Fe_2O_5$. Moreover, the investigation of the magnetic properties shows that differently from $Pb_{2-x}Ba_xFe_2O_5$, this oxide is not antiferromagnetic, but exhibits a spin glasslike behavior below $T_g \simeq 0$ K.

EXPERIMENTAL SECTION

Synthesis. The oxide $Pb_{1.3}Ba_{0.7}MnFeO_5$ was prepared by solid state reaction of PbO, Mn_2O_3, Fe_2O_3, and $BaCO_3$. The stoichiometric amounts of these oxides and carbonate were intimately ground in an agate mortar and first heated at 750 °C in a platinum crucible in an argon flow for 12 h. The reacted mixtures were then ground again, pressed into pellets under 200 MPa, heated up to 850 °C at 5 °C/min, and maintained at this temperature for 12 h in an argon flow.

X-ray Powder Diffraction (XRPD) and Neutron Powder Diffraction (NPD). X-ray powder diffraction patterns were collected on a Bruker D8 diffractometer using Cu−Kα_1 radiation (1.54056 Å), selected by an incident germanium monochromator, and equipped with a Lynx-Eye. The diagrams were collected at room temperature in a continuous scan mode with a step scan of ~0.011°/2θ ranging from 10 to 150°/2θ. Neutron powder diffraction (NPD) data collection was carried out on the 3T2 diffractometer (wavelength $\lambda = 1.22515$ Å) at room temperature at the Laboratoire Léon Brillouin (LLB) at Saclay.

Transmission Electron Microscopy Characterization. Conventional TEM studies including electron diffraction (ED) and high

Received: February 18, 2013
Published: May 8, 2013

resolution TEM (HRTEM) analyses were performed on microcrystalline samples, using a Tecnai G2 30 UT microscope with a 0.17 nm point resolution, operated at 300 kV. The TEM samples were prepared by mechanical crushing in an agate mortar; the samples were suspended in methanol and spread over holey carbon films. Aberration-corrected HAADF-STEM and STEM-EDX experiments were carried out on a JEOL −ARM 200 F cold FEG double-corrected microscope operated at 200 kV, equipped with Centurio EDX detector.

Magnetic Measurements. The d.c. magnetization measurements were performed using a superconducting quantum interference device (SQUID) magnetometer with a variable temperature cryostat (Quantum Design, San Diego, USA). All the d.c. measurements were carried out in an applied field of 0.3 T. The a.c. susceptibility, $\chi_{ac}(T)$ was measured with a PPMS (Quantum Design, San Diego, USA) with the frequency ranging from 10 Hz to 10 kHz. In the a.c. measurements, the H_{ac} and H_{dc} fields were kept fixed at 10 and 0 Oe, respectively. All the magnetic properties were registered on dense ceramic bars of dimensions ~4 × 2 × 2 mm^3.

■ RESULTS AND DISCUSSION

Structure Solution. The structure of $Pb_{1.3}Ba_{0.7}MnFeO_5$ was first investigated from room temperature X-ray powder diffraction data. The indexation performed with DICVOL06[9] gives an orthorhombic unit-cell with parameters a = 5.7914 Å; b = 3.8888 Å; c = 21.4064 Å and figure of merit M(20) = 183.2 (0.0019, 64). These unit-cell parameters were then confirmed from electron diffraction experiments. A first pattern matching of the experimental X-ray powder diffraction diagram, on the basis of the cell determined from electron diffraction studies, was performed with the program JANA2006[10] in space group *Pmmm*. A careful observation of the indexed pattern showed that all (0*kl*) reflections with $k + l = 2n + 1$ and all (*hk*0) reflections with $h = 2n + 1$ are systematically absent. These reflection conditions are consistent with space groups *Pnma* (centrosymetric) and $Pn2_1a$ (noncentrosymetric). The extraction of the structure factors using the Le Bail method[11] was carried out with the JANA2006 in the centrosymetric space group *Pnma*. The structure was solved using EXPO2004.[12] The best solution was obtained with a reliability factor of $R_F = 0.011$ and crystallographic positions for Pb, Ba, Fe(× 2) were directly found as well as five positions for the oxygen atoms. The corresponding formula was then assumed to be $PbBaFe_2O_5$. Subsequent Rietveld refinements of this model were performed with JANA2006. Since no distinction between Fe and Mn atoms is available from XRPD data, the first series refinements were done assuming mixed occupancies 50%-Fe/50%-Mn for the two concerned crystallographic positions. The refinements of the isotropic atomic displacement parameters (APD) for heavier atoms (Pb, Ba, Fe/Mn) converged to a very small value for the Ba atom position, showing a lack of electron on this position. We decided then to consider this position as occupied by a mixed atom Ba/Pb. To be consistent with the nominal composition $Pb_{1.3}Ba_{0.7}FeMnO_5$ the starting occupancy ratio was 0.65/0.35, and the refinements of these occupancy parameters were done assuming that their sum should be equal to one and lead to the following formula: $Pb_{1.28}Ba_{0.72}FeMnO_5$.

The structure was finally refined from neutron powder diffraction (NPD) data to distinguish the iron atoms from the manganese atoms since their neutron scattering lengths are quite different: 9.45 × 10^{-15} m and −3.73 × 10^{-15} m for Fe and Mn, respectively. The occupancy factors Fe/Mn were refined for the two concerned crystallographic positions assuming to keep their overall sum equal to one for both positions. Anisotropic strain broadening of peaks was corrected by the tensor method,[13] and peak asymmetry due to axial divergence was also corrected according to the Finger, Cox & Jephcoat approach.[14] The final refinement converged with reliability factors of RB_{obs} = 0.0376, R_{wp} = 0.0301; GOF = 1.95 and gives a chemical formula of $Pb_{1.26(4)}Ba_{0.74(4)}Fe_{1.03(3)}Mn_{0.97(3)}O_5$, very close to the nominal formula. The resulting NPD diagram is shown in Figure 1.

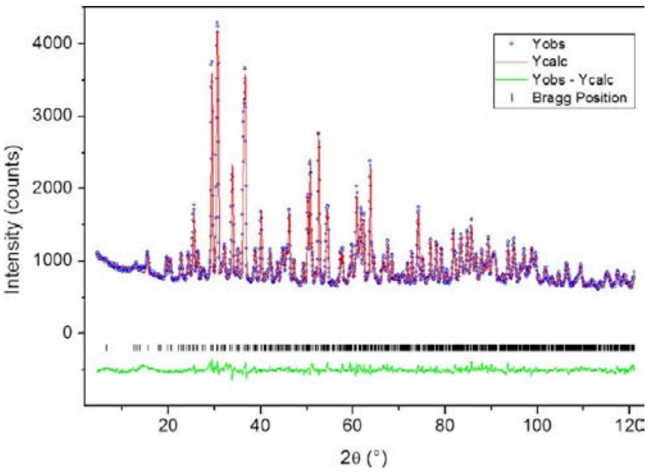

Figure 1. Powder neutron diffraction pattern of $Pb_{1.26}Ba_{0.74}MnFeO_5$ with Rietveld refinement results (calculated and difference profiles).

Further details of powder data collections and refinements are summarized in Table 1. Atomic coordinates and isotropic

Table 1. Details of Neutron Powder Diffraction Data and Structure Refinement of $Pb_{1.3}Ba_{0.7}FeMnO_5$

diffractometer	3T2 − Laboratoire Léon Brillouin - Saclay
radiation/wavelength (Å)	neutron/1.22515
angular range (°2θ)	4.58−121.03
step size (°2θ)	0.05
temperature (°C)	20
asymmetry correction	Axial divergence - Finger, Cox & Jephcoat
background	12 Legendre polynoms
anisotropic strain broadening	Stephens
space group/no.	*Pnma*/62
formula units *Z*	4
a (Å)	5.7897(4)
b (Å)	3.8925(3)
c (Å)	21.4036(17)
V (Å^3)	482.36(8)
formula sum	Pb1.26(4) Ba0.74(4) Fe1.03(3) Mn0.97(3) O5
formula weight	556.1
X-ray density/g·cm^{-3}	7.6556
Rietveld agreement indices	
derived Bragg *R*-factor, R_{Bobs}	0.0376
profile, R_p	0.0238
weighted profile, R_{wp}	0.0301
corrected profile, cR_p	0.0894
GOF	1.94
CSD no.	425753

Table 2. Atomic Positions and Isotropic Displacement Parameters of $Pb_{1.3}Ba_{0.7}FeMnO_5$

atoms	position Wyckoff	occupancy	x	y	z	U (Å^2)
Pb1	4c	1	0.0464(13)	0.25	0.5707(2)	0.0109(12)
Pb2	4c	0.26(4)	0.562(2)	0.25	0.6873(5)	0.014(3)
Ba2	4c	0.74(4)	0.562(2)	0.25	0.6873(5)	0.014(3)
Fe1	4c	0.603(14)	0.465(2)	0.25	0.4427(5)	0.001(3)
Mn1	4c	0.397(14)	0.465(2)	0.25	0.4427(5)	0.001(3)
Fe2	4c	0.426(12)	0.921(5)	0.25	0.3100(13)	0.003(6)
Mn2	4c	0.574(12)	0.921(5)	0.25	0.3100(13)	0.003(6)
O1	4c	1	0.056(2)	0.25	0.6766(4)	0.009(2)
O2	4c	1	0.676(2)	0.25	0.2476(6)	0.014(3)
O3	4c	1	0.5746(19)	0.25	0.5346(4)	0.012(2)
O4	4c	1	0.1931(17)	0.25	0.3932(5)	0.010(2)
O5	4c	1	0.7047(19)	0.25	0.3861(5)	0.013(2)

Table 3. Selected Interatomic Distances of $Pb_{1.3}Ba_{0.7}FeMnO_5$

atoms	distance (Å)	atoms	distance (Å)
Pb1−O1	2.267(10)	Fe1/Mn1−O5	1.843(16)
Pb1−O4 (× 2)	2.512(8)	Fe1/Mn1−O4	1.897(16)
Pb1−O5 (× 2)	2.592(9)	Fe1/Mn1−O3 (× 2)	2.019(4)
Pb1−O3	2.839(13)	Fe1/Mn1−O3	2.068(14)
Ba2/Pb2−O2 (× 2)	2.762(12)	Mn2/Fe2−O2	1.92(3)
Ba2/Pb2−O2 (× 2)	2.783(12)	Mn2/Fe2−O2	1.95(3)
Ba2/Pb2−O1	2.871(18)	Mn2/Fe2−O1 (× 2)	1.972(5)
Ba2/Pb2−O1	2.912(14)	Mn2/Fe2−O5	2.05(3)
Ba2/Pb2−O1	2.937(18)	Mn2/Fe2−O4	2.38(3)
Ba2/Pb2−O5 (× 2)	2.940(12)		
Ba2/Pb2−O4	2.961(11) (× 2)		

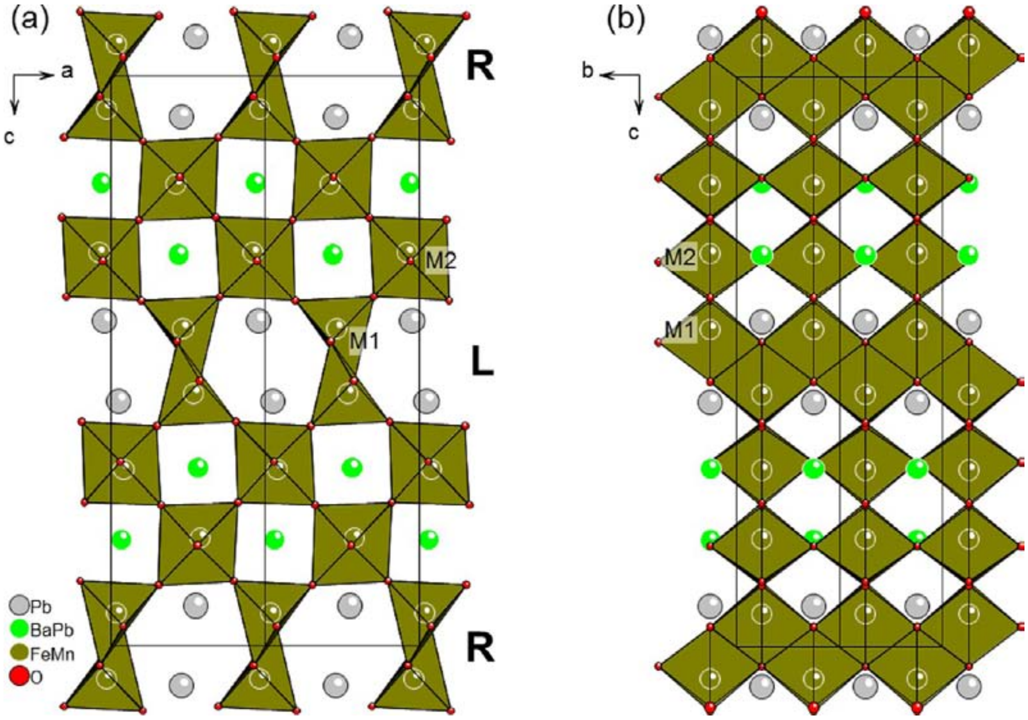

Figure 2. View of the structure of $Pb_{1.3}Ba_{0.7}MnFeO_5$ (a) along the *b*-axis and (b) along the *a*-axis.

displacement parameters of the structures of $Pb_{1.3}Ba_{0.7}FeMnO_5$ are given in Table 2. Selected interatomic distances and angles of the two structures are summarized in Table 3. Drawings of structural details were produced using the software DIAMOND.[15]

Additional crystallographic information on each structure can be obtained from Fachinformationszentrum Karlsruhe, D-76344 Eggenstein-Leopoldshafen, Germany, E-mail: crysdata@fiz-karlsruhe.de, by quoting the reference and the CSD numbers 425753.

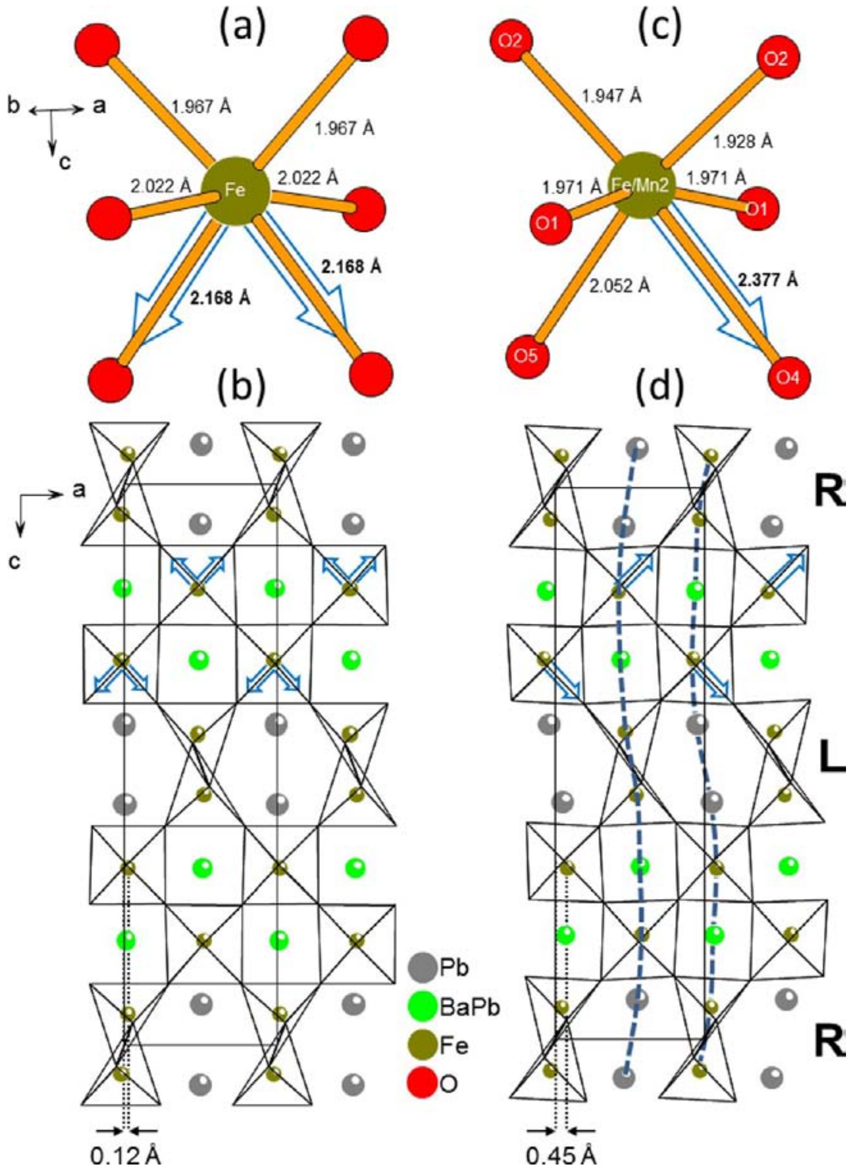

Figure 3. Influence of the different MO_6 distortions on $Pb_{2-x}Ba_xFe_{2-y}Mn_yO_5$ structures. (a) FeO_6 octahedron present in (b) $PbBaFe_2O_5$ structure. (c) Fe/MnO_6 octahedron present in (d) $Pb_{1.3}Ba_{0.7}MnFeO_5$ structure. The blue dotted lines show the zigzag rows with an Pb−Fe/Mn−Ba/Pb−Fe/Mn sequence. The blue arrows show the longer M−O bonds in MO_6 octahedra.

Structure Description. The projections of the crystal structure of $Pb_{1.3}Ba_{0.7}FeMnO_5$ (Figure 2) show its great similarity with the parent oxides $Pb_{2-x}Ba_xFe_2O_5$,[5,6,8] and $Pb_{1.33}Sr_{0.67}Fe_2O_5$,[1] previously described. Like for the ferrites of this structural family, the $[MnFeO_5]_\propto$ framework consists of double perovskite layers, where corner-shared MO_6 octahedra (labeled M2) are statistically occupied by Mn^{3+} (∼58%) and Fe^{3+} (42%). Similar to the corresponding ferrites, the perovskites layers are interconnected through ribbons of edge-sharing MO_5 polyhedra (labeled M1), running along $\vec{b}$. The MO_5 polyhedra are also statistically occupied by Mn^{3+} (∼40%) and Fe^{3+} (∼60%), and exhibit a geometry intermediate between that of a trigonal bipyramid and that of a tetragonal pyramid, which will be discussed further. The $[MnFeO_5]_\alpha$ framework forms six-sided tunnels occupied by Pb^{2+} cations exclusively, whereas the perovskite cages are preferentially occupied by Ba^{2+} cations (74%). As observed in the series of compounds $Pb_{2-x}Ba_xFe_2O_5$[5] and $Pb_{1.33}Sr_{0.67}Fe_2O_5$,[1] no tilts are observed for the MO_6 octahedra in the perovskite blocks of $Pb_{1.3}Ba_{0.7}FeMnO_5$. Nevertheless, the $[MnFeO_5]_\propto$ framework (Figure 3d) differs from the $[Fe_2O_5]_\propto$ framework of $Pb_{2-x}Ba_xFe_2O_5$ (Figure 3b) comparing the distortions of the MO_6 octahedra in the perovskite blocks. Within the $[Fe_2O_5]_\propto$ framework, the FeO_6 octahedra (Figure 3a) present two longer Fe−O bonds including the two types of oxygen atoms common to the octahedra and trigonal bipyramids FeO_5. As a consequence, Fe^{3+} exhibits, in the octahedral (001) layers, a 4 + 2 coordination which can be described as a tetrahedral distortion of the FeO_6 octahedra. Thus, in the pure iron oxide $Pb_{2-x}Ba_xFe_2O_5$, the Fe−O bonds that ensure the cohesion between the (001) layers of FeO_5 pyramids and the layers of FeO_6 octahedra are ∼0.16 Å larger than all the other Fe−O bonds of the structure. This ability of Fe^{3+} to go toward the tetrahedral coordination allows a relaxation of the strains along $\vec{c}$ between the octahedral and pyramidal layers of the structure. In the case of the $[MnFeO_5]_\alpha$ framework, the MO_6 octahedra (Figure 3c) exhibit only one longer M−O bond (Fe/Mn2−O4 = 2.377 Å); the latter corresponds to the O4 atom shared

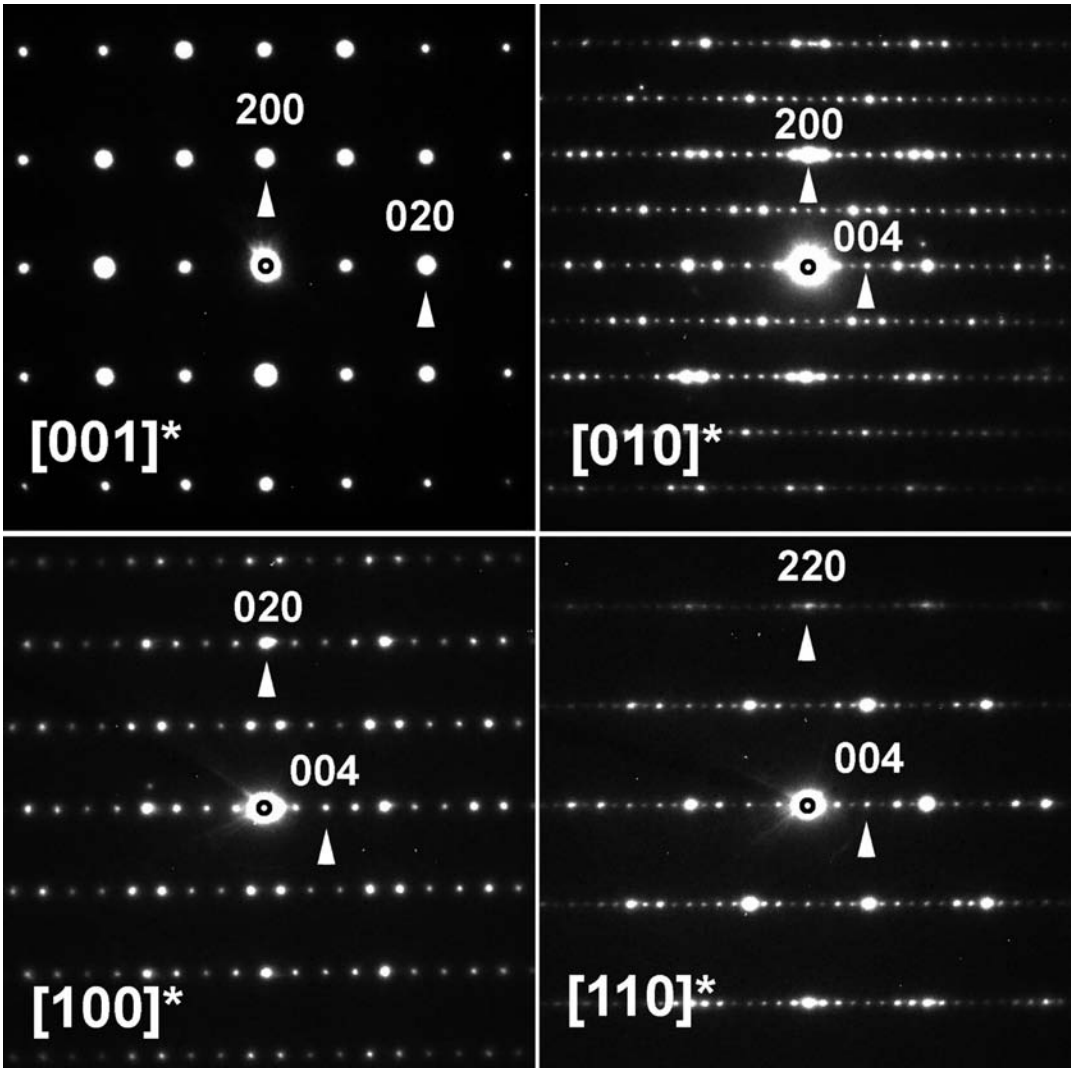

Figure 4. Electron diffraction patterns of four main reciprocal zones of $Pb_{1.3}Ba_{0.7}MnFeO_5$.

between the (Fe/Mn2)O_6 octahedra and the (Fe/Mn1)O_5 pyramids (Figure 3d). Thus, the (Fe/Mn2)O_6 octahedra in this structure show a 5 + 1 coordination, which can be described as a tetragonal pyramidal distortion. Such a feature can easily be explained by the presence in those sites of Mn^{3+}, which tends to impose either the presence of elongated MnO_6 octahedra or of MnO_5 tetragonal pyramids due to its Jahn−Teller effect. As a consequence, Fe/Mn2−O4 larger distances appear between the (001) layers of (Fe/Mn1)O_5 pyramids and the layers of (Fe/Mn2)O_6 pyramidally distorted octahedra. Moreover, those distances are significantly larger, ~0.32 Å, than all the other Fe/Mn−O bonds of the structure. Nevertheless, one M-O distance out of two at the interface of the pyramidal and octahedral layers (Fe/Mn_2−O5 = 2.052 Å) remains short. (Figure 3c,d) This suggests that such a pyramidal distortion of the octahedra induces significant strains in the structure compared to pure iron oxides. This viewpoint is supported by the fact that the pure manganese oxides $Pb_2Mn_2O_5$ with a similar structure[8] can only be synthesized under high pressure. A detailed refinement of the structure of the high pressure synthesized $Pb_2Mn_2O_5$ would be necessary to check this statement.

This different distortion of the Mn/FeO_6 octahedra compared to the pure FeO_6 octahedra of the $PbBaFe_2O_5$ structure induces a large displacement of the Fe/Mn2 cations along $\vec{a}$. The latter can be estimated by considering the structure of the high temperature (HT) form of $PbBaFe_2O_5$[5] which exhibits the most symmetric double perovskite layers in these compounds, where Fe2 atoms occupy the 0, 1/4, *z* crystallographic position instead of *x*, 1/4, *z* in the low temperature (LT) forms of $Pb_2BaFe_2O_5$, in $Pb_{1.33}Sr_{0.67}Fe_2O_5$,[1] and in $Pb_{1.3}Ba_{0.7}FeMnO_5$. Thus, the displacement of the corresponding Fe2 atom along $\vec{a}$ is ~0.12 Å in the low temperature (LT) structure $PbBaFe_2O_5$ as well as in $Pb_{1.28}Ba_{0.72}Fe_2O_5$[6] and ~0.18 Å in $Pb_{1.33}Sr_{0.67}Fe_2O_5$ structure against ~0.45 Å in $Pb_{1.3}Ba_{0.7}FeMnO_5$. This displacement of the Fe/Mn2 atom type, followed by its surrounding oxygen atoms, causes then the displacement in the same direction of the other atoms Pb1, Ba/Pb2, Fe/Mn1 in order to satisfy correct coordinations. Indeed, one observes that the cationic (100) layers Pb1, Fe/Mn_2, Ba, Fe/Mn1 (dotted blue line in Figure 3b,d), which are practically planar in the $PbBaFe_2O_5$ structure (Figure 3b), are waving in the $Pb_{1.3}Ba_{0.7}FeMnO_5$ structure (Figure 3d). As a consequence, the "Pb_2" pairs in the six-sided tunnels of this manganoferrite are no more aligned along $\vec{c}$, but are alternately tilted along $\vec{a}$. Thus, in the *Pnma* space group the presence of the glide plane perpendicular to $\vec{c}$ imposes two configurations of the "Pb_2" pairs in the six-sided tunnels: "Pb_2" pairs tilted left (L) and right (R) along $\vec{a}$. These two configurations of the "Pb_2" pairs are also observed for the pairs of edge-sharing pyramids $(MO_5)_2$, since the Fe/Mn1 atoms are also shifted along $\vec{a}$. In a common layer parallel to the (ab) plane L "Pb_2" pairs alternate with L $(MO_5)_2$, pairs forming an L type layer and R Pb-pairs alternate with R $(MO_5)_2$, forming an R type layer. Along $\vec{c}$ L layers and R layers alternate with an L-R-L-R sequence. These features can be also deduced from HRTEM images as will be presented further, and were also observed in the HREM study of $Pb_2Mn_2O_5$,[8] but in the latter case the atomic displacements were only calculated from a structural model since the structure could not be refined. As previously indicated, the geometry of the $(Fe/Mn1)O_5$ polyhedra can be described as intermediate between a trigonal bipyramid and a tetragonal pyramid. For those polyhedra, the Fe/Mn1−O distances ranging from 1.843(17) to 2.070(15) Å are similar to those observed in the $Pb_{2-x}Ba_xFe_2O_5$ compounds.[5,6] Nevertheless, for the LT structure of $PbBaFe_2O_5$, Nikolaev et al.[5] have described those FeO_5 polyhedra as trigonal bipyramids rather than tetragonal pyramids with an O5−Fe1−O3 angle between the trigonal base and the apical O3 atom of 99.9°. The same value (99.8°) is observed for the corresponding angle in the $Pb_{1.28}Ba_{0.72}Fe_2O_5$ structure.[6] In $Pb_{1.3}Ba_{0.7}FeMnO_5$ structure the O5−Fe/Mn1−O3 angle increases to 104.1°. This strongly suggests that the presence of Mn^{3+} in the MO_5 polyhedra of the $Pb_{1.26}Ba_{0.74}MnFeO_5$ structure induces a significant distortion of their configuration tending toward a coordination of the Fe^{3+}/Mn^{3+} cations closer to a tetragonal pyramid. As also mentioned by Nikolaev et al,[5] the phase transition between the HT and LT structure of $PbBaFe_2O_5$ implies the possibility to move the O3 atoms toward the a axis, with the Fe1 atom keeping the distorted trigonal bipyramidal coordination. For $Pb_{1.3}Ba_{0.7}FeMnO_5$, no phase transition is observed at high temperature. It seems that the presence of Mn^{3+} in the MO_5 polyhedra hinders the displacement of the O3 atoms, in agreement with the higher ability of Mn^{3+} to accommodate a tetragonal pyramidal coordination due to its Jahn−Teller behavior.

High Resolution Transmission Electron Microscopy (HRTEM) Study. The ED patterns of the $Pb_{1.26}Ba_{0.74}MnFeO_5$ were obtained for four most relevant zone axis: [001]*, [010]*, [100]*, and [110]* (Figure 4). All ED patterns were completely indexed on an orthorhombic *Pnma* (62) space group with the following unit cell parameters: a = 5.79 Å, b = 3.89 Å, c = 21.4 Å, which are in good agreement with those obtained from XRD. No superstructure spots due to a possible Fe−Mn ordering were detected in the ED patterns.

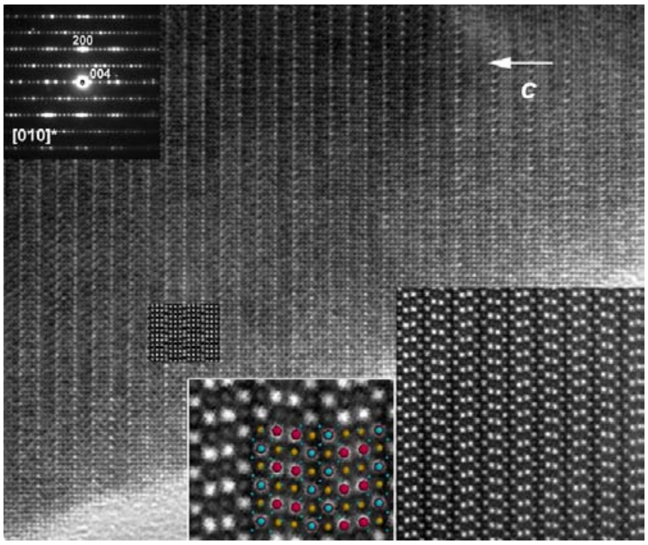

Figure 5. Bright−field [010] HRTEM image of $Pb_{1.26}Ba_{0.74}MnFeO_5$ and corresponding ED pattern. Image simulation for $\Delta f = -25$ nm and t = 4.8 nm is given as an inset. High resolution HAADF-STEM image acquired along the same zone axis for $Pb_{1.26}Ba_{0.74}MnFeO_5$ crystal is given as inset in the right bottom corner. The corresponding structural model is overlaid onto a magnified HAADF-STEM image (Pb- red; Ba/Pb- big light blue; Mn/Fe- yellow; O- small light blue).

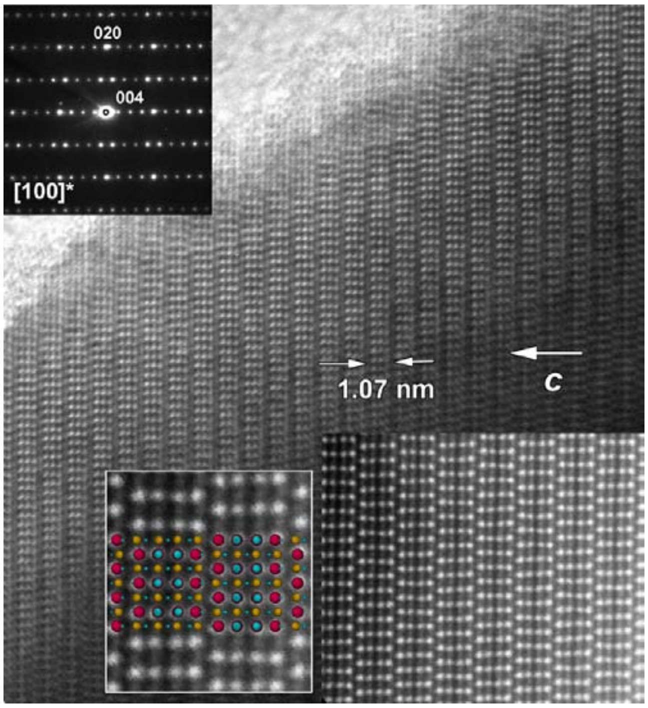

Figure 6. Bright field [100] HRTEM image of $Pb_{1.26}Ba_{0.74}MnFeO_5$ and corresponding ED pattern. Image simulation for $\Delta f = -20$ nm and t = 2.4 nm is given as an inset. High resolution HAADF-STEM image acquired along the same zone axis for $Pb_{1.26}Ba_{0.74}MnFeO_5$ crystal is given as insert in the right bottom corner. The corresponding structural model is overlaid onto magnified HAADF-STEM image (Pb- red; Ba/Pb- big light blue; Mn/Fe- yellow; O- small light blue).

The HRTEM study of $Pb_{1.3}Ba_{0.7}MnFeO_5$ was performed along two relevant and most informative zone axis, [100] and [010], respectively. The bright field HRTEM images along [100] (Figure 5) and along the [010] zone axis (Figure 6) together with the corresponding HAAD-STEM images show the perfectly crystallized and homogeneous nature of the samples. HRTEM image simulations based on the *Pnma* crystal structure obtained from NPD data are given as an inset for both zone axis and show a good correspondence with experimental images. According to the image simulation, in the HRTEM image the dark dots correspond to the cationic positions, and white dots represent the channels and oxygen columns. In the HAADF-STEM images, where the contrast is directly proportional to the atomic number ($\sim Z^2$), the brightest dots are correlated to the heaviest Pb (Z = 82) atoms, whereas less bright dots correspond to Ba (Z = 56) atoms. The weak bright dots in between the brightest correspond to the Fe (Z = 26) and Mn (Z = 25) columns. Thereby, the zigzag bright dots in the [010] HAADF-STEM image (Figure 6) indicate the positions of the perovskite layers, which consist of corner-sharing MO_6 octahedra (M = Fe/Mn), whereas Ba(Pb) cations

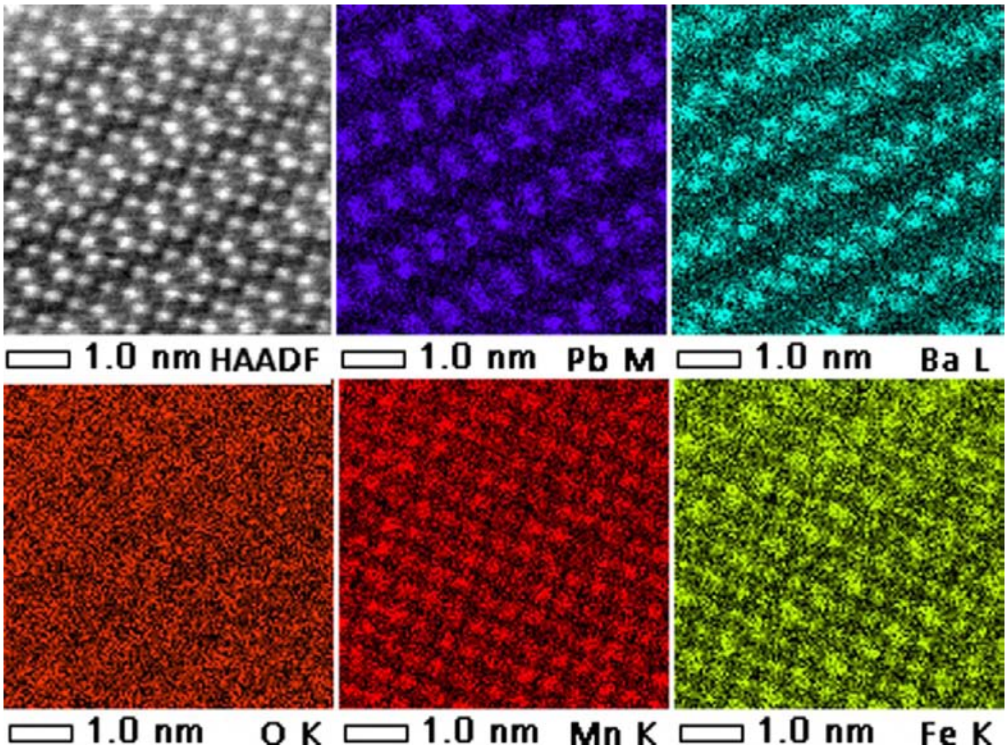

Figure 7. Selected high resolution HAADF image (upper corner) along the [010] zone axis and corresponding atomic EDX elemental maping of Pb$_{1.26}$Ba$_{0.74}$MnFeO$_5$ crystal for all elements: Pb, Ba, O, Mn, and Fe.

sit in the tunnels of perovskite blocks (see overlay structural model in inset Figure 6). Similarly, bright contrast dumbbells represent the pairs of Pb^{2+} cations (Pb$_2$) located inside each six-sided tunnel built up of edge-sharing MO$_5$ tetragonal pyramids, imaged as weak bright dots of Fe(Mn) atomic columns and connected to perovskite blocks. Note that the "Pb$_2$" pairs are not parallel along $\vec{c}$ but are alternatively tilted left (L) and right (R) with respect to the *c* axis, in agreement with the results of the structure determination from NPD data (Figure 3), which emphasizes the significant difference with respect to pure ferrites Pb$_{2-x}$Ba$_x$Fe$_2$O$_5$.[5,6]

As stated above, HRTEM and HAAD-STEM images show an uniform contrast free of any modulations, suggesting a good crystallinity of the material and a regular layer stacking along the *c*-axis. Thus, the ED and HRTEM study does not give any evidence of possible Fe−Mn local ordering or superstructures. In order to get more information about the Fe/Mn and Pb/Ba atoms positions in the structure, the atomic-resolution STEM-HAADF chemical mapping using energy-dispersive X-ray (EDX) spectroscopy was applied. A two-dimensional chemical mapping for Pb$_{1.3}$Ba$_{0.7}$MnFeO$_5$ along the [010] zone axis is shown in Figure 7 for all the elements. The agreement and correspondence between the [010] Pb$_{1.3}$Ba$_{0.7}$MnFeO$_5$ projected structure, the EDS maps, and the HAADF image are excellent. The Fe and Mn atomic maps confirm the NPD results: there is no preferential position for Fe or Mn. These cations are distributed randomly within the same octahedral and pyramidal layers. So, there is no evidence of chemical segregation or ordering, which is in agreement with ED and HRTEM results. Appearing on the Pb map, the weak contrast of the dots in the positions of the Ba atoms suggests the presence of small amounts of Pb atoms in the perovskite cages. This intermixing of the Pb^{2+} and Ba^{2+} cations has also been demonstrated by the NPD study. In spite of the fact that numerous microcrystals exhibit a perfect crystal structure, a systematic and careful HRTEM observation of different samples of this material along the [010] zone axis has revealed the presence of extended defects running along $\vec{a}$. Note that these defects are difficult to detect when the crystallite is perfectly [010] oriented and a little tilting out of the [010] zone is required in order to increase the contrast difference between two successive (001) layers of MO$_5$ tetragonal pyramids containing the dumbbell "Pb$_2$" pairs. Such a slightly misoriented [010] HRTEM image of a defect region is shown in Figure 8a. One observes that, for these imaging conditions the contrast between two successive (001) layers of dumbbell "Pb$_2$" pairs is much more pronounced; i.e., if one layer is imaged as dumbbells of different brightness (labeled for instance L), the next layer will be imaging as a line of single bright dots (labeled for instance R). Thus, the perfect structure (Figure 2a) which consists of "Pb$_2$"-(001) successive layers along $\vec{c}$ that are alternately oriented left (L) and right (R) will be imaged as an alternative sequence of these two types of contrast layers "L-R-L-R..." which are definitely present in the largest part of the image. However, besides this regular "L-R-L-R..." sequence, one observes stacking faults along $\vec{c}$. These stacking faults can be described by the fact that two successive "Pb$_2$" layers exhibit the same contrast without any shift of the dot columns (Figure 8b). These extended defects are also observed in Pb$_2$Mn$_2$O$_5$[8] and can be interpreted as antiphase boundaries (APB). In both compounds Pb$_2$Mn$_2$O$_5$ and Pb$_{1.3}$Ba$_{0.7}$MnFeO$_5$, the APB are always located in the middle of a (001) double perovskite layer and separate two parts of the structure displaced by 1/2[111] as shown in Figure 8c. Bearing in mind that the EDX mapping shows a random distribution of Fe and Mn species, and that the contrast is similar for each "Pb$_2$" layer, image simulations could be carried out for these extended defects (Figure 8c) showing that they can be

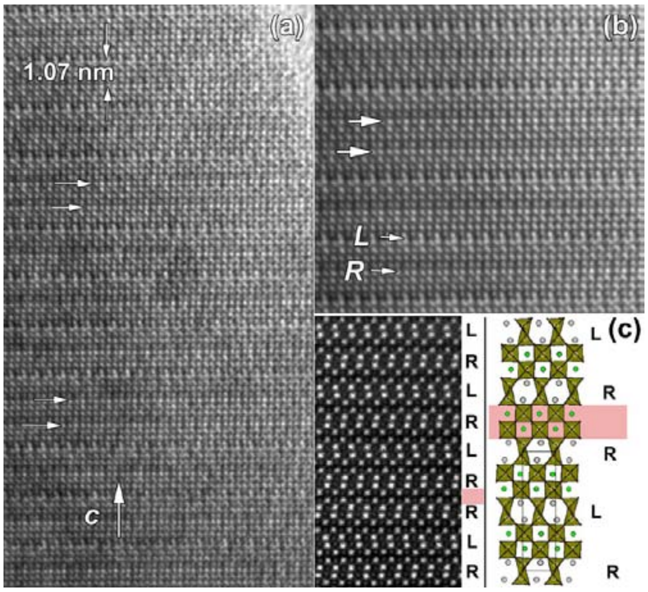

Figure 8. (a) Bright field [010] HRTEM image evidence showing the formation of double rows of similar contrast layers within the $Pb_{1.3}Ba_{0.7}MnFeO_5$ crystal; (b) enlarged image of the stacking fault area, double layers of similar contrast indicated by white arrows; (c) high resolution HAADF-STEM image of defect region and corresponding structural model of double layer defect where L- and R- is notation of left and right tilted Pb dumbbells with respect to the *c*-plane correspondingly.

expressed as the local sequence "L-R-R-L". The [010] HAADF-STEM image (Figure 8c) reveals indeed the appearance of two layers of similar orientation (R-R) corresponding to bright contrast dumbbells (Pb columns) within a "L-R-L-R..."matrix. Note that the ED studies did not allow any extra spots to be detected along [001] in any crystallite suggesting that no long-range ordering of such extended defects takes place in the matrix. The absence of any intensity modulation confirms that the defect is purely structural and has no chemical substitution nature.

Magnetic Properties. Temperature-dependent d.c. magnetization of $Pb_{1.3}Ba_{0.7}FeMnO_5$ measurements under an applied d.c. magnetic field of 0.3 T in both the zero-field-cool (ZFC) and field-cooled (FC) conditions is shown in Figure 9a. On cooling, the FC curve shows a monotonous increase with the decrease in temperature except a small jump around 60 K (Figure 9a). Moreover, the ZFC curve starts splitting from the FC curve below 60 K, and on further lowering the temperature, it exhibits a pronounced peak below ~40 K, marked as T_f in Figure 9a). The high temperature paramagnetic phase follows the Curie−Weiss law as can be seen from the linear fit to inverse susceptibility data above 70 K (inset of Figure 9a). The Curie constant, effective moment and Curie−Weiss temperature (θ_{CW}) obtained from the linear fit are 17.23 emu·K/f.u., 11.79 μ_B/f.u. and −114 K, respectively. The observed moment is in good agreement with calculated spin only moment obtained from the relation $\mu_{cal} = \{3\,\mu^2_{Fe^{3+}} + 3\,\mu^2_{Mn^{3+}}\}^{1/2} = 13.31$ μ_B for the high spin moments of $\mu_{Fe^{3+}} = 5.92$ μ_B and $\mu_{Mn^{3+}} = 4.90$ μ_B. The negative θ_{CW} indicates the existence of antiferromagnetic correlation in the high temperature phase.

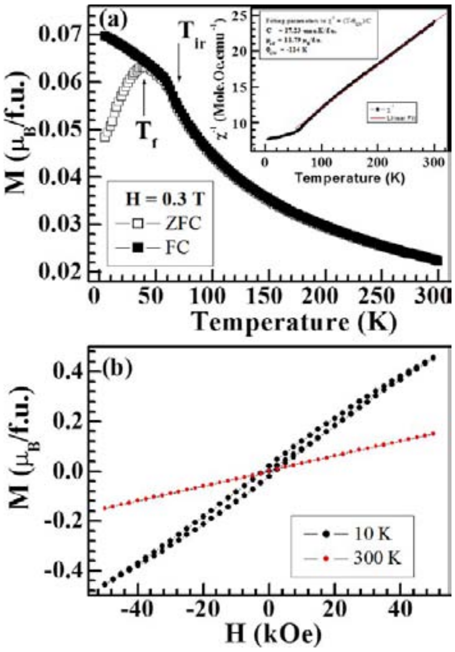

Figure 9. (a) ZFC and FC dc magnetization curves of $Pb_{1.3}Ba_{0.7}MnFeO_5$ measured under an applied field of 0.3 T. Inset shows the inverse susceptibility plot fitted with Curie−Weiss law along with the fitting parameters. (b) *M* vs *H* curves recorded at 10 and 300 K up to ±5 T.

The splitting of ZFC and FC curves signifies the onset of magnetic irreversibility at a temperature, defined as T_{ir} below which ZFC and FC curves break up. The observation of a peak in the ZFC curve and a clear separation of the ZFC and FC curves at T_{ir} are typical characteristics of spin glass materials.[16] These features are commonly ascribed to spin freezing or spin ordering resulting in a spin glass like phase formation at lower temperatures. However, the splitting of the ZFC and FC curves is not sufficient to conclude to the spin glass nature of the system, as it can be seen even in ferromagnetic regime due to domain wall pinning effect.[17] The isothermal magnetization, *M*−*H* curves measured at 10 and 300 K are shown in Figure 9b. The linear *M*−*H* curve at 300 K is typical of a paramagnetic material. The same curve at 10 K shows nonlinearity with a significant hysteresis loop, which is not closed even at ±5 T and remains unsaturated, a feature characteristic of spin glass.[18] In order to confirm the spin glass feature of $Pb_{1.3}Ba_{0.7}FeMnO_5$, we have performed dynamic susceptibility measurements for a wide range of frequency between 10 Hz and 10 kHz. Figure 10

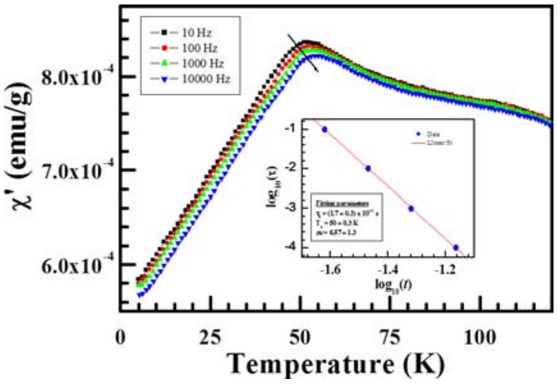

Figure 10. $\chi'_{ac}(T)$ curves of $Pb_{1.3}Ba_{0.7}MnFeO_5$ measured as a function of temperature at different frequencies ranging between 10 Hz to 10 kHz. Inset show plots of $\log_{10}\tau$ vs $\log_{10}(t)$, where $t = (T_f - T_g)/T_g$. Solid line is linear fit to the data (see text for details).

shows the temperature-dependent $\chi'(T)$ curve for $Pb_{1.3}Ba_{0.7}FeMnO_5$, revealing a clear shift in peak position to higher temperature and a concomitant decrease in amplitude with the increase in frequency. Such a frequency dispersion of the low temperature susceptibility peak indicates the presence of short-range magnetic interactions. A variation in $T_f \sim 51.4$ K (10 Hz) to ~53.2 K (10 kHz) from our measurement leads to a peak shift per decade of frequency, $p = ((\Delta T_f/T_f)/(\Delta \log f))$ ~0.017, where T_f is the freezing temperature taken as the peak position on the $\chi'(T)$ curve. This value matches well with those of the classical spin glass (~0.001−0.08).[19] This has been substantiated by analyzing the frequency dependence of the peak in χ' using the conventional power law model of spin dynamics:[20] $\tau = \tau_0((T_f - T_g)/(T_g))^{-z\nu}$, where T_f is the frequency-dependent freezing temperature, T_g is the critical temperature for spin glass ordering which is equivalent to the freezing temperature T_f at $f \rightarrow 0$, and τ_0 is the characteristic time scale for spin dynamics. $z\nu$ is the critical exponent typically ranging from 5 to 12. In the inset in Figure 10 we have shown the best fit to the data in the frequency range 10 Hz to 10 kHz with the fitting parameters $T_g = 50 \pm 0.3$ K, $z\nu = 6.57 \pm 1.3$, and $\tau_0 \sim 10^{-12}$ s. These values are in good agreement with those for well-known spin glasses. This suggests that the spin glass behavior in $Pb_{1.3}Ba_{0.7}FeMnO_5$ can be well described using critical slowing down model.

Such a spin glass behavior has previously been observed for single perovskite[21] and double perovskite[22] oxides, due to cationic disordering in the octahedral framework. For the present system, we suggest that the antiferromagnetic ordering observed in the perovskite $Pb_{2-x}Ba_xFe_2O_5$[5] is destroyed by the disordering introduced by the Mn^{3+} cations distributed at random on the Fe^{3+} sites of the $Pb_{2-x}Ba_xFe_2O_5$. The antiferromagnetic exchange interactions between Fe^{3+} and Mn^{3+} ions, i.e., Fe^{3+}−O−Fe^{3+}, Mn^{3+}−O−Mn^{3+}, and Fe^{3+}−O−Mn^{3+} in randomly distributed corner shared octahedral and square pyramidal sites lead to the disruption of long-range antiferromagnetic ordering resulting in a spin glass phase. The blocking of robust orbital correlated long-range A-type antiferromagnetic ordering in Fe^{3+} substituted manganites $La_{0.66}Ba_{0.40}Mn_{0.61}Fe_{0.33}O_3$ has been attributed to the exchange disorder which prevents the long-range spin ordered state.[23] In the present system, the anisotropic environment of Fe^{3+} and Mn^{3+} will further promote the disorder exchange, facilitating the formation of a glassy state.

CONCLUSIONS

This study of the oxide $Pb_{2-x}Ba_xMnFeO_5$ shows that up to 50% of Mn^{3+} can be substituted for Fe^{3+}, at random in the $Pb_{2-x}Ba_xFe_2O_5$ matrix, due to the ability of these two cations to accommodate both the 5-fold and the octahedral coordination simultaneously. It is this cationic disordering between Mn^{3+} and Fe^{3+} in the different sites of the structure which cancels the antiferromagnetic behavior observed in the $Pb_{2-x}Ba_xFe_2O_5$ matrix[5] and generates spin glass behavior for $Pb_{2-x}Ba_xFeMnO_5$. Importantly, one observes that, in spite of this similarity between Fe^{3+} and Mn^{3+}, the crystal chemistry of these mixed "Mn−Fe" oxides is governed by the different structural behaviors of Mn^{3+} and Fe^{3+} cations. Indeed, the former, due to its Jahn−Teller properties, tends to form tetragonal MnO_5 pyramids, and consequently in $Pb_{1.3}Ba_{0.7}FeMnO_5$ the (Fe/Mn)O_6 octahedra exhibit a strong tetragonal pyramidal distortion (Fe/Mn)O_{5+1} and the MO_5 pyramids at the junction between two perovskite layers tend toward a more pronounced tetragonal pyramidal configuration. In contrast, for the pure iron ferrites $Pb_{2-x}Ba_xFe_2O_5$, the FeO_6 octahedra exhibit a significant tetrahedral distortion FeO_{4+2}, whereas the FeO_5 polyhedra at the junction of two perovskite layers tend toward a trigonal bipyramidal configuration. The great flexibility of this structure opens the route to the design of new members characterized by various thicknesses of the perovskite layers.

ASSOCIATED CONTENT

Supporting Information

This material is available free of charge via the Internet at http://pubs.acs.org.

AUTHOR INFORMATION

Corresponding Author

*E-mail: nicolas.barrier@ensicaen.fr.

Present Address

§On leave from Department of Chemistry, Visva-Bharati University, Santiniketan-731235, India.

Notes

The authors declare no competing financial interest.

ACKNOWLEDGMENTS

The authors are particular grateful to Dr. E. Okunishi (JEOL Ltd.) for the help in performing HAADF and atomic EDX mapping experiments.

REFERENCES

(1) Raynova-Schwarten, V.; Massa, W.; Babel, D. *Z. Anorg. Allgem. Chem.* **1997**, *623*, 1048.
(2) Bertaut, F.; Blum, P.; Sagnieres, A. *C. R. Acad. Sci.* **1957**, *244*, 2944; *Acta Crystallogr.* **1959**, *12*, 149.
(3) Greaves, C.; Jacobson, A. J.; Tofield, B. C.; Fender, B. E. *Acta Crystallogr. B* **1975**, *31*, 641.
(4) Abakumov, A. M.; Hadermann, J.; Bals, S.; Nikolaev, I. V.; Antipov, E. V.; Van Tendeloo, G. *Angew Chem., Int. Ed.* **2006**, *45*, 6697. Hadermann, J.; Abakumov, A. M.; Nikolaev, I. V.; Antipov, E. V.; Van Tendeloo, G. *Solid State Sci.* **2008**, *10*, 382.
(5) Nikolaev, I. V.; D'Hondt, H.; Abakumov, A. M.; Hadermann, J.; Balagurov, A.; Bobrikov, I. A.; Sheptyakov, D. V.; Pomjakushin, V. Y.; Pokholok, K. V.; Filimonov, D. S.; Van Tendeloo, G.; Antipov, E. V. *Phys. Rev.* **2008**, *B78*, 24426.
(6) Tzvetkov, P.; Petrova, N.; Kovacheva, D. *J. Alloys Comp.* **2009**, *485*, 862.
(7) Bougerol, C.; Gorius, M. F.; Grey, I. E. *J. Solid State Chem.* **2002**, *169*, 131.
(8) Hadermann, J.; Abakumov, A. M.; Perkisas, T.; D'Hondt, H.; Tan, H.; Verbeecka, J.; Filonenko, V. P.; Antipov, E. V.; Van Tendeloo, G. *J. Solid State Chem.* **2010**, *183*, 2190.
(9) Boultif, A.; Louer, D. *J. Appl. Crystallogr.* **2004**, *37*, 724.
(10) Petrícek, V.; Dušek, M.; Palatinus, L. *Crystallographic Computing System JANA2006*; Institute of Physics, Academy of Sciences of the Czech Republic: Prague, 2006.
(11) Le Bail, A.; Duroy, H.; Fourquet, J. L. *Mater. Res. Bull.* **1988**, *23*, 447.
(12) Altomare, A.; Caliandor, R.; Camalli, M.; Cuocci, C.; Giacovazzo, C.; Moliterni, A. G. G.; Rizzi, R. *J. Appl. Crystallogr.* **2004**, *37*, 1025.
(13) Stephens, P. W. *J. Appl. Crystallogr.* **1999**, *32*, 281.
(14) Finger, L. W.; Cox, D. E.; Jephcoat, A. P. *J. Appl. Crystallogr.* **1994**, *27*, 892.
(15) Brandenburg, K. *DIAMOND*, Version 3.2i; Crystal Impact: Germany, 1999
(16) Binder, K.; Young, A. P. *Rev. Mod. Phys.* **1986**, *58*, 801.

(17) Dho, J.; Kim, W. S.; Hur, N. H. *Phys. Rev. Lett.* **2002**, *89*, 027202.

(18) Binder, K.; Young, A. P. *Rev. Mod. Phys.* **1986**, *58*, 801.

(19) Binder, K.; Young, A. P. *Rev. Mod. Phys.* **1986**, *58*, 801. Mydosh, J. A. *Spin Glass: An Experimental Introduction*; Taylor & Francis: London, 1993.

(20) Hohenberg, P. C.; Halperin, B. I. *Rev. Mod. Phys.* **1977**, *49*, 435. Mydosh, J. A. *Spin Glass: An Experimental Introduction*; Taylor & Francis: London, 1993.

(21) Bréard, Y.; Hardy, V.; Raveau, B.; Maignan, A.; Lin, H.-J.; Jang, L.-Y.; Hsieh, H. H.; Chen, C. T. *J. Phys.: Condens. Matter* **2007**, *19*, 216212.

(22) Poddar, A.; Bhowmik, R. N.; Muthuselvam, I. P.; Das, N. J. *Appl. Phys.* **2009**, *106*, 073908. Greedan, J. E.; Derakhshan, S.; Ramezanipour, F.; Siewenie, J.; Proffen, Th. *J. Phys.: Condens. Matter* **2011**, *23*, 164213.

(23) Granado, R.; Urbano, R.; Perez, C. A.; Azimonte, C.; Lynn, J. W.; Souza, R. A.; Souza-Neto, N. M.; Ramos, E. A. Y.; Bychkov, G. L.; Shiryaev, S. V.; Barilo, S. N. *Phys. Rev. B* **2005**, *72*, 052406.